



CLASSICAL AND PREDICTIVE CONTROL APPLIED TO A DC/DC BOOST CONVERTER

Santiago Cortés-Perdomo, Sergio A. Rincón-Caupaz and Diego F. Sendoya-Losada
 Department of Electronic Engineering, Faculty of Engineering, Surcolombiana University, Neiva, Huila, Colombia
 E-Mail: diego.sendoya@usco.edu.co

ABSTRACT

In this work, two controllers, a Proportional Integral (PI) and a Model-based Predictive Controller (MPC), have been designed to regulate a DC/DC Boost converter. First, the modeling and linearization of the system was performed using a frequency response estimation method. Then the PI controller was designed around a certain setpoint. Next, an algorithm was designed according to the Extended Prediction Self-Adaptive Control (EPSAC). Finally, the performance of the controllers is evaluated for setpoint tracking and disturbance rejection.

Keywords: boost converter, EPSAC, MPC, PI, RMSE.

1. INTRODUCTION

The DC/DC converter is an electrical circuit that transfers energy from a DC voltage source to a load. The energy is first transferred via electronic switches to energy storage devices and then subsequently switched from storage into the load. The switches are transistors and diodes; the storage devices are inductors and capacitors. This process of energy transfer results in an output voltage that is related to the input voltage by the duty ratios of the switches.

DC/DC converters have applications in various areas such as Telecommunications, Industrial Robotics, Aerospace & Defense, Medical, Consumer and Automotive, among others. DC/DC converters are used in portable electronic devices such as mobile phones and laptops, which are mainly powered by batteries. Such electronic devices often contain multiple sub-circuits, each with its own voltage level requirement different from that supplied by the battery or external source. For example, a lithium battery powers a laptop computer, and several DC/DC converters change the battery voltage into the voltages required by the loads. A buck converter produces the low-voltage dc required by the microprocessor. A boost converter increases the battery voltage to the level needed by the disk drive. In a power system of an earth-orbiting spacecraft, a solar array produces the main power bus voltage. DC/DC converters convert bus voltage to the regulated voltages required by the spacecraft payloads. Battery charge/discharge controllers interface the main power bus to batteries; these controllers may also contain DC/DC converters.

Due to its importance and large number of application areas, the Alternative Energy Research Seedbed of the Surcolombiana University, is investigating various control techniques that allow obtaining a specific and regulated output voltage for various types of DC/DC converters. In the literature, a large amount of information related to the analysis, design, and control of DC/DC converters can be found that use classical and advanced techniques to control voltage, current or duty cycle, and, in this way, maintain a proper functioning of the circuit in different situations [1-11].

In this contribution, Model-based Predictive Control (MPC) is applied to a Boost converter, in which a Single-Input Single-Output (SISO) system configuration has been considered. The circuit is powered with an input voltage of 12 V, the output voltage is the controlled variable and the duty cycle is the manipulated variable. Usually the control of the linear systems is done by classical control techniques such as PI, due to its well-known and simple structure. For the design of these conventional controllers it is necessary to choose a setpoint and then to find a linear model of the system, ensuring that the control works well in this region, but when it moves away from the setpoint, the controller loses effectiveness. In this contribution, the Extended Predictive Self-Adaptive Control (EPSAC) algorithm is used to setpoint tracking and disturbance rejection. Then a comparison is made with the classic PI control to demonstrate the effectiveness of the proposed algorithm. The performance of these controllers is tested and evaluated in a simulation environment. Simulation is done using Matlab®/Simulink® software.

2. MATERIALS AND METHODS

2.1 Process Model

The circuit shown in Figure-1 is called a boost converter because the output voltage is larger than the input.

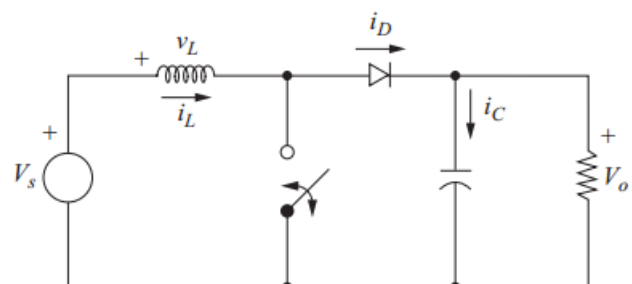


Figure-1. Schematic of boost converter.



The boost DC/DC converter has the following parameters: $V_s = 12V$, $L = 120\mu H$, $C = 48\mu F$, $R = 50 \Omega$. When the switching frequency $f = 25KHz$ and $D = 0.6$, the following open-loop response is obtained.

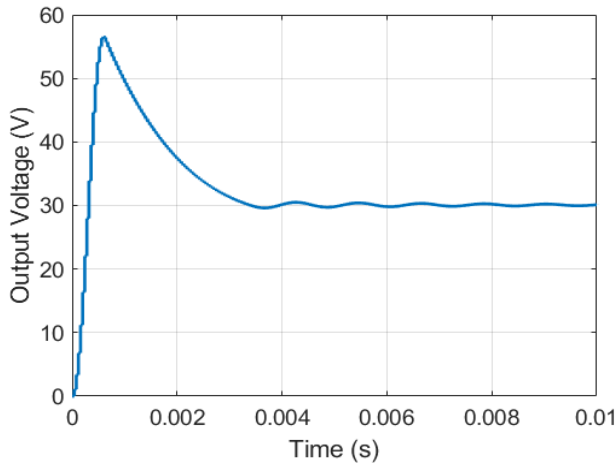


Figure-2. Open-loop response.

It can be seen that the output voltage has an overshoot $OS = 88.236\%$ and a settling time $t_s = 3.2ms$. The steady-state output voltage $V_o = 30V$. Therefore, a controller is required to improve the performance of the closed-loop system. The design of the controller requires a mathematical representation of the circuit.

Analysis of the boost converter begins by making these assumptions:

- The circuit is operating in the steady-state.
- The inductor current is continuous (always positive).
- The capacitor is very large, and the output voltage is held constant at voltage V_o .
- The switching period is T ; the switch is closed for time DT and open for time $(1 - D)T$.
- The components are ideal.

The key to the analysis for determining the output V_o is to examine the inductor current and inductor voltage first for the switch closed and then for the switch open. The net change in inductor current over one period must be zero for steady-state operation. The average inductor voltage is zero.

Analysis for the Switch Closed: When the switch is closed in the boost converter circuit of Figure-1, the diode is reverse-biased. The voltage across the inductor is:

$$v_L = V_s = L \frac{di_L}{dt} \quad (1)$$

$$\frac{di_L}{dt} = \frac{V_s}{L} \quad (2)$$

Since the derivative of the current is a positive constant, the current increases linearly. The change in

current while the switch is closed is computed by modifying the preceding equation.

$$\frac{di_L}{dt} = \frac{\Delta i_L}{\Delta t} = \frac{\Delta i_L}{DT} = \frac{V_s}{L} \quad (3)$$

$$(\Delta i_L)_{\text{closed}} = \left(\frac{V_s}{L}\right) DT \quad (4)$$

Analysis for the Switch Open: When the switch is open, the inductor current cannot change instantaneously, so the diode becomes forward-biased to provide a path for the inductor current. The voltage across the inductor when the switch is open is:

$$v_L = V_s - V_o = L \frac{di_L}{dt} \quad (5)$$

$$\frac{di_L}{dt} = \frac{V_s - V_o}{L} \quad (6)$$

The derivative of current in the inductor is a negative constant and the current decreases linearly. The change in inductor current when the switch is open is:

$$\frac{di_L}{dt} = \frac{\Delta i_L}{\Delta t} = \frac{\Delta i_L}{(1-D)T} = \frac{V_s - V_o}{L} \quad (7)$$

$$(\Delta i_L)_{\text{open}} = \left(\frac{V_s - V_o}{L}\right) (1 - D)T \quad (8)$$

Steady-state operation requires that the inductor current at the end of the switching cycle be the same as that at the beginning, meaning that the net change in inductor current over one period is zero. This requires:

$$(\Delta i_L)_{\text{closed}} + (\Delta i_L)_{\text{open}} = 0 \quad (9)$$

$$\left(\frac{V_s}{L}\right) DT + \left(\frac{V_s - V_o}{L}\right) (1 - D)T = 0 \quad (10)$$

Solving for V_o :

$$V_o = \frac{V_s}{1-D} \quad (11)$$

The boost converter produces an output voltage that is greater than or equal to the input voltage.

In order to obtain a mathematical model that represents the dynamics between V_o and D , a chirp signal is used to make the duty cycle vary sinusoidally with amplitude between 0.59 and 0.61, from a frequency of 20 Hz to 3 KHz. These changes originate an output voltage that also changes sinusoidally, which makes it possible to construct a Bode diagram (Figure-3) and, in this way, to estimate the transfer function between V_o and D .

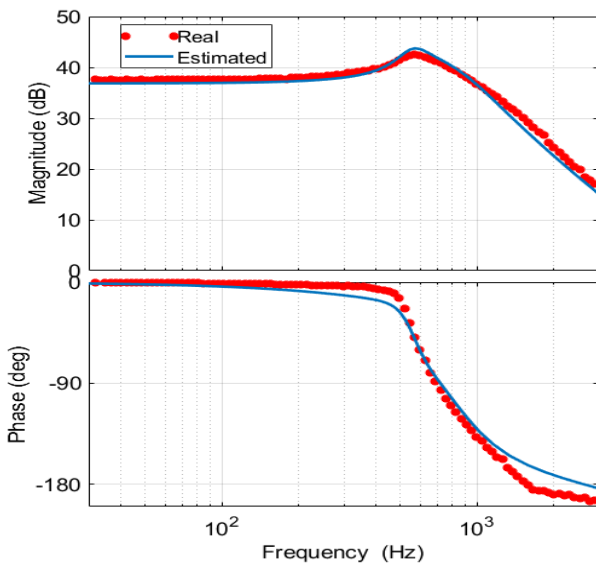


Figure-3. Bode plot for transfer function estimation.

This transfer function is a linear representation of the system at setpoint of 30 V, with a fit to estimation data of 82.05%:

$$\frac{V_o(s)}{D(s)} = \frac{-2.621e04s^3 + 1.802e09s^2 + 3.365e12s + 2.258e16}{s^4 + 5406s^3 + 4.354e07s^2 + 8.376e10s + 3.249e14} \quad (12)$$

2.2 PI Controller Design

To improve the behavior of the closed-loop system, a PI controller is initially designed. The design criteria were that the controlled system output had the minimum settling time and overshoot, and that the PI controller output was between 0 and 1, which corresponds to the limits of the duty cycle.

The algorithm that describes the behavior of the PI controller is:

$$u(t) = K_p e(t) + K_i \int_0^t e(\tau) d\tau \quad (13)$$

$u(t)$ is the output signal of the PI controller, which in this case corresponds to the duty cycle. $e(t)$ is the input signal of the PI controller, which is defined as $e(t) = r(t) - y(t)$, where $r(t)$ is the setpoint and $y(t)$ is the output of the process, that is, the output voltage. K_p is the proportional gain and K_i is the integral gain [12-16].

Applying the Laplace transform, the transfer function of the PI controller is found:

$$\frac{U(s)}{E(s)} = K_p + \frac{K_i}{s} = 0.0057 + \frac{17.0976}{s} \quad (14)$$

2.3 EPSAC

It is common practice in MPC to structure the future control scenario. At each current moment t , the process output $y(t+k)$ is predicted over a time horizon $k = 1 \dots N_2$. The predicted values are indicated by $y(t+k|t)$ and the value N_2 is called the prediction horizon. A prediction horizon $N_2 = 3$ is used in this work. The prediction model used is given in (12). The forecast

depends on the past inputs and outputs, but also on the future control scenario $u(t+k|t)$ with $k = 0 \dots N_2 - 1$. This can be done by defining a control horizon N_u with $1 \leq N_u \leq N_2$, after which the control strategy remains constant, i.e. $u(t+k|t) = u(t+N_u-1|t)$ for $N_u \leq k \leq N_2 - 1$ [17].

Conceptually the future response $y(t+k|t)$ can be considered as the cumulative result of 2 effects: $y_{base}(t+k|t)$, which is calculated based on the effect of future disturbances $n(t+k|t)$, the effect of past control $u(t-1), u(t-2), \dots$ and the effect of a basic future control scenario $u_{base}(t+k|t)$ with $k = 0 \dots N_2 - 1$; and $y_{opt}(t+k|t)$, which is the effect of the optimizing future control actions $\delta u(t+k|t)$ with $k = 0 \dots N_2 - 1$, i.e. $\delta u(t+k|t) = u(t+k|t) - u_{base}(t+k|t)$, where $u(t+k|t)$ is the optimal control input that is sought [18].

Structuring leads to simplified calculations by reducing the degrees of freedom of the control vector from N_2 to N_u and generally has a positive effect on robustness. The extremely simplified version $N_u = 1$ leads to remarkably good results in many practical applications [19]. Hence, a control horizon $N_u = 1$ is used in this work. The control horizon implies that $u_{base}(t+k|t) = u_{base}(t|t)$ and $\delta u(t+k|t) = \delta u(t|t)$ for $1 \leq k \leq N_2 - 1$. Furthermore, $y_{opt}(t+k|t)$ -being the result of $\delta u(t+k|t)$ - is the effect of a single step input with amplitude $\delta u(t|t)$ at time t . The system output at time $t+k$ is thus, $y_{opt}(t+k|t) = g_k \delta u(t|t)$ for $1 \leq k \leq N_2$, where g_k for $k = 1 \dots N_2$ are the coefficients of the unit step response of the system [20].

For a linear system with constant parameters, the step response coefficients are constant and thus must be calculated only once. Using matrix notation, $Y_{opt} = GU$:

$$\begin{bmatrix} y_{opt}(t+1|t) \\ y_{opt}(t+2|t) \\ \dots \\ y_{opt}(t+N_2|t) \end{bmatrix} = \begin{bmatrix} g_1 \\ g_2 \\ \dots \\ g_{N_2} \end{bmatrix} \delta u(t|t) \quad (15)$$

The key EPSAC equation is then $Y = Y_{base} + Y_{opt}$. The task of the controller is to find the control vector $u(t+k|t)$ with $k = 0 \dots N_2 - 1$ that minimizes the cost function:

$$\sum_{k=N_1}^{N_2} [r(t+k|t) - y(t+k|t)]^2 = (R - Y)^T (R - Y) \quad (16)$$

where the default value for N_1 is the systems time delay, $N_1 = 1$ is used in this work. $r(t+k|t)$ is the reference trajectory, which is in this case the setpoint R . Minimization of (16) with respect to U gives the optimal solution:

$$U^* = (G^T G)^{-1} G^T (R - Y_{base}) \quad (17)$$

Since the control horizon is chosen $N_u = 1$, the matrix $G^T G$ with dimensions $N_u \times N_u$ is a scalar and thus its inversion has a low computational cost. The actual



control action applied to the real process at the current time t is $u(t) = u_{\text{base}}(t|t) + \delta u(t|t)$, i.e.:

$$u(t) = u_{\text{base}}(t|t) + U^*(1) \quad (18)$$

At the next sampling instant $t + 1$, the whole procedure is repeated by considering the new measurement information $y(t + 1)$ (so-called receding horizon) [21].

Clipping is applied to the control action whenever necessary because the limits of the duty cycle are between 0 and 1.

3. RESULTS AND DISCUSSIONS

The simulation was conducted towards two scenarios to compare the behavior of the PI and EPSAC algorithms. The performance of the controllers is evaluated, in order to carry out a tracking to a reference voltage and an effective rejection of the disturbances.

3.1 Scenario 1: Disturbance Rejection

In order to evaluate the performance of the controlled system when a disturbance is applied, the voltage reference or setpoint is fixed at 30 V.

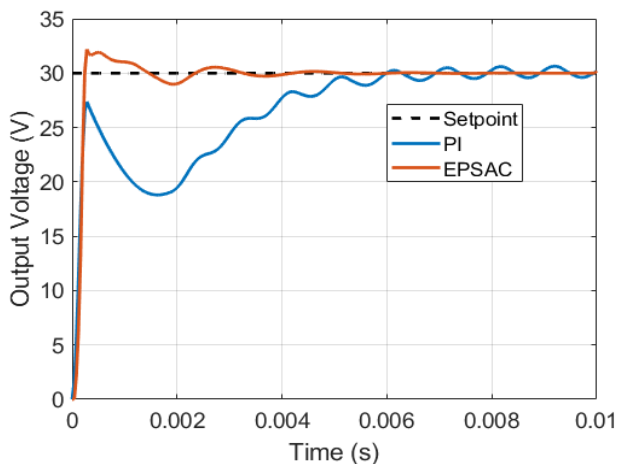


Figure-4. Closed-loop response.

It can be seen that when the PI controller is used, the closed-loop response presents no overshoot ($OS = 0\%$), but the settling time increases with respect to the open-loop response ($t_s = 5.8\text{ms}$). Even the steady-state response exhibits small oscillations around the setpoint. On the other hand, when the EPSAC algorithm is used, the response presents an overshoot and a settling time lower than those observed in open-loop ($OS = 7.33\%$ and $t_s = 2.1\text{ms}$).

Figure-5 shows the control actions developed by each controller. Initially, the control effort of the EPSAC algorithm is greater than that of the PI controller, which explains the higher response speed in closed-loop. As steady-state is reached, the two controllers deliver the same duty cycle $D = 0.6$.

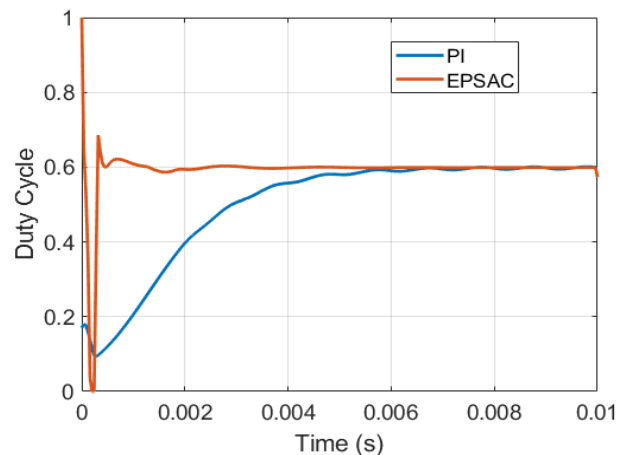


Figure-5. Duty cycle with PI and EPSAC algorithms.

After the response reaches the steady-state a disturbance is applied to the system, which consists of a change in the input voltage, that is, V_s goes from 12 V to 14 V at 10 ms. Finally, when the response reaches the steady-state again, the input voltage is changed from 14 V to 10 V at 20 ms. Figure-6 shows the output voltage when PI and EPSAC (prediction horizon $N_2 = 3$) algorithms are used. This prediction horizon is used because it allows the response to have the shortest settling time with a small overshoot.

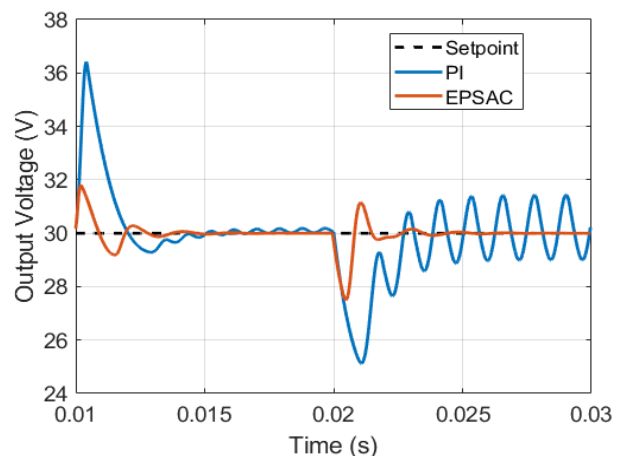


Figure-6. Disturbance rejection.

It can be seen that when the PI controller is used, the rejection of the disturbance is not very effective, since the response in steady-state presents sustained oscillations in both cases. On the other hand, when the EPSAC algorithm is used, the steady-state is achieved 1.68ms after the first disturbance is applied, and 1.28ms after the second disturbance is applied.

Figure-7 shows that when the first disturbance is applied at 10 ms, both algorithms reduce the duty cycle from 0.6 to 0.53, however the output of the PI controller shows small sustained oscillations. When the second disturbance is applied at 20 ms, both algorithms increase the duty cycle from 0.53 to 0.67. Again, oscillations in the output of the PI controller are observed.

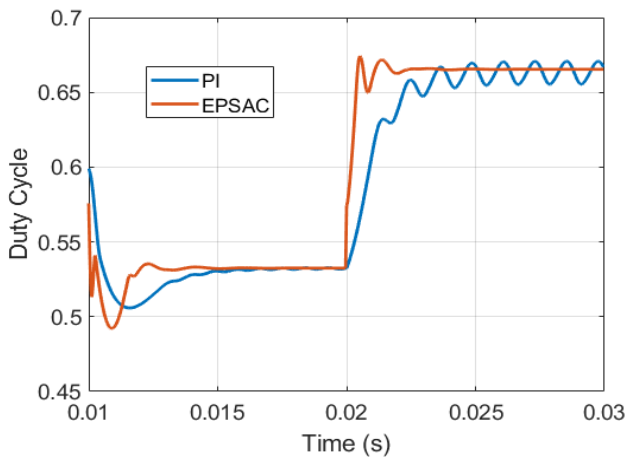


Figure-7. Duty cycle for disturbance rejection with PI and EPSAC algorithms.

3.2 Scenario 2: Setpoint Tracking

In order to evaluate how the system behaves in closed-loop at different setpoints, a voltage reference signal composed of 3 steps with amplitudes of 30 V, 36 V, and 24 V is applied. Figure-8 shows how the process output $y(t)$ tracks a setpoint for a prediction horizon $N_2 = 3$.

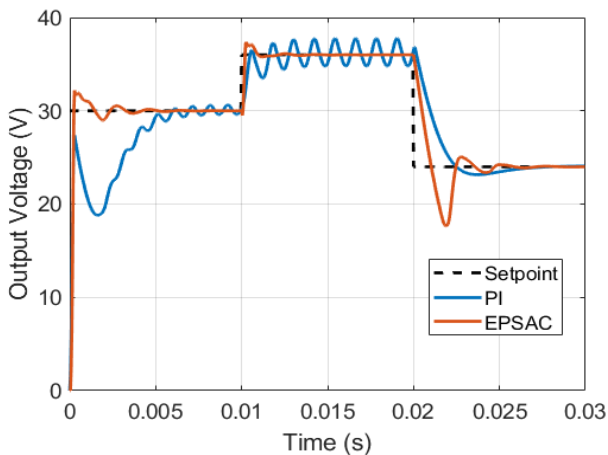


Figure-8. Setpoint tracking.

For the reference voltage of 30 V, it can be seen that when the PI controller is used, the closed-loop response presents no overshoot ($OS = 0\%$), but the settling time increases with respect to the open-loop response ($t_s = 5.8\text{ms}$). Even the steady-state response exhibits small oscillations around the setpoint. On the other hand, when the EPSAC algorithm is used, the response presents an overshoot and a settling time lower than those observed in open-loop ($OS = 7.33\%$ and $t_s = 2.1\text{ms}$). At 10 ms, when the reference voltage is increased to 36 V, it can be seen that the closed-loop response, when the PI controller is used, presents a greater overshoot ($OS = 4.78\%$), but the output voltage never stabilizes and exhibits sustained oscillations around 36 V. On the other hand, when the EPSAC algorithm is used, the response presents an overshoot and a settling time lower than those

observed in open-loop ($OS = 3.81\%$ and $t_s = 0.72\text{ms}$). Finally, at 20 ms, when the reference voltage decreases to 24 V, it can be seen that the closed-loop response, when the PI controller is used, does not have a significant undershoot ($US = 3.5\%$), but the settling time is larger ($t_s = 5.2\text{ms}$). On the other hand, when the EPSAC algorithm is used, the response has a larger undershoot and settling time ($US = 26.5\%$ and $t_s = 4.48\text{ms}$).

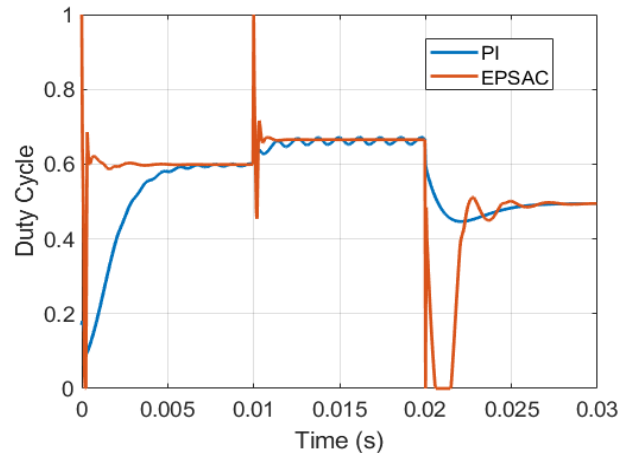


Figure-9. Duty cycle for setpoint tracking with PI and EPSAC algorithms.

Figure-9 shows the control actions performed by each controller. Initially, the control effort of the EPSAC algorithm is greater than that of the PI controller, which explains the higher response speed in closed-loop. As steady-state is reached, the two controllers deliver the same duty cycle $D = 0.6$. At 10 ms, both algorithms increase the duty cycle from 0.6 to 0.67, however the output of the PI controller shows sustained oscillations. At 20 ms, both algorithms reduce the duty cycle from 0.67 to 0.49. In all cases, it can be seen that the variations in the useful cycle originated by the EPSAC algorithm are more pronounced than those of the PI controller, which allows faster changes in the output voltage.

3.3 RMSE

In order to obtain a detailed results analysis of the comparative study between the PI and EPSAC algorithms, the Root Mean Square Error (RMSE) variations were used.

$$RMSE = \sqrt{\frac{\sum_{t=1}^N [r(t)-y(t)]^2}{N}} \tag{19}$$

where $r(t)$ is the setpoint signal, $y(t)$ is the output signal, and N is the number of samples. Figure-10 shows that the quality of the response is much better when the EPSAC algorithm is used.

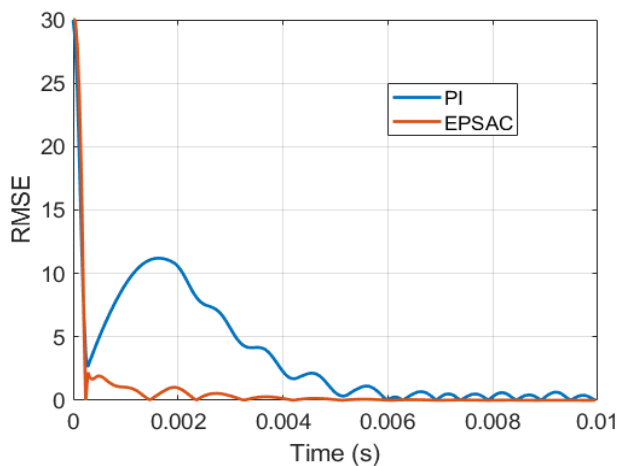


Figure-10. RMSE variations for PI and EPSAC algorithms.

Table-1 shows the RMSE variations for both the PI controller and the EPSAC algorithm when the two simulation scenarios are applied.

Table-1. RMSE variations for PI and EPSAC.

| Scenario | PI (%) | EPSAC (%) |
|----------|--------|-----------|
| 1 | 7.47 | 2.41 |
| 2 | 86.23 | 11.98 |

The implemented EPSAC algorithm presents a better behavior in the two scenarios compared to the PI algorithm.

Although the computational cost of the implementation of the EPSAC algorithm is higher, the system response is noticeably faster than when the PI controller is used. This can be an advantage in systems where it is necessary to minimize the values of overshoot and settling time. However, for processes where these requirements are not necessary, the PI algorithm would be more viable because of its simplicity of implementation.

4. CONCLUSIONS

In this work, the performance of PI and EPSAC algorithms was evaluated. It can be observed that the EPSAC is more effective in rejecting disturbances. This is because changes in the duty cycle are more pronounced when there are changes in the input voltage. In the same way, because the EPSAC uses the linear model of the plant to make the predictions, then the tracking to the variations in the reference voltage is much better. In addition, the control effort required is greater when changing from one setpoint to another.

REFERENCES

[1] Zhu Y. and W. Xiao. 2020. A comprehensive review of topologies for photovoltaic I-V curve tracer. *Solar Energy*. 196: 346-357.

[2] Rehman, Zubair, Ibrahim Al-Bahadly and Subhas Mukhopadhyay. 2015. Multiinput DC-DC converters in renewable energy applications-An overview. *Renewable and Sustainable Energy Reviews*. 41: 521-539.

[3] Sivakumar S., *et al.* 2016. An assessment on performance of DC-DC converters for renewable energy applications. *Renewable and Sustainable Energy Reviews*. 58: 1475-1485.

[4] Khosrogorji S., *et al.* 2016. Multi-input DC/DC converters in connection with distributed generation units-A review. *Renewable and sustainable energy reviews*. 66: 360-379.

[5] Zhang Neng, Danny Sutanto and Kashem M. Muttaqi. 2016. A review of topologies of three-port DC-DC converters for the integration of renewable energy and energy storage system. *Renewable and Sustainable Energy Reviews*. 56: 388-401.

[6] Revathi, B. Sri and M. Prabhakar. 2016. Non isolated high gain DC-DC converter topologies for PV applications-A comprehensive review. *Renewable and Sustainable Energy Reviews*. 66: 920-933.

[7] Arunkumari T. and V. Indragandhi. 2017. An overview of high voltage conversion ratio DC-DC converter configurations used in DC micro-grid architectures. *Renewable and Sustainable Energy Reviews*. 77: 670-687.

[8] Singh S. N. 2017. Selection of non-isolated DC-DC converters for solar photovoltaic system. *Renewable and Sustainable Energy Reviews*. 76: 1230-1247.

[9] Gopi, R. Reshma and S. Sreejith. 2018. Converter topologies in photovoltaic applications-A review. *Renewable and Sustainable Energy Reviews*. 94: 1-14.

[10] Hossain M. Z. and N. A. Rahim. 2018. Recent progress and development on power DC-DC converter topology, control, design and applications: A review. *Renewable and Sustainable Energy Reviews*. 81: 205-230.

[11] Amir, Asim, *et al.* 2019. Comparative analysis of high voltage gain DC-DC converter topologies for photovoltaic systems. *Renewable energy*. 136: 1147-1163.



- [12] Sendoya-Losada Diego F., Vargas-Duque Diana C. and Ávila-Plazas Ingrid J. 2018. Implementation of a neural control system based on PI control for a non-linear process. 2018 IEEE 1st Colombian Conference on Applications in Computational Intelligence (ColCACI). IEEE.
- [13] Sendoya-Losada Diego F. and Quintero-Polanco Jesús D. 2018. Control of yaw angle in a miniature helicopter. ARPJ Journal of Engineering and Applied Sciences. 13: 620-626.
- [14] Sendoya-Losada Diego F. and Quintero-Polanco Jesús D. 2018. PID controller applied to an unmanned aerial vehicle. ARPJ Journal of Engineering and Applied Sciences. 13: 325-334.
- [15] Sendoya-Losada Diego F. and Quintero-Polanco Jesús D. 2018. Design and validation of a pid auto-tuning algorithm. ARPJ Journal of Engineering and Applied Sciences. 13: 3797-3802.
- [16] Sendoya-Losada Diego F. 2018. KCR PID auto-tuner algorithm applied to a FOT device. ARPJ Journal of Engineering and Applied Sciences. 13: 2505-2510.
- [17] Sendoya-Losada D. F. 2019. Principles, applications and perspectives of predictive control. ARPJ Journal of Engineering and Applied Sciences. 14: 2464-2467.
- [18] Sendoya-Losada D.F., Robayo Betancourt, Faiber, and Salgado Patrón, José. 2017. Application of a predictive controller with variable time delay in general anesthesia. ARPJ Journal of Engineering and Applied Sciences. 12: 2661-2667.
- [19] Sendoya-Losada Diego F. and Molina Mosquera Johan J. 2017. Linear and nonlinear predictive control algorithms applied to a heated tank system. ARPJ Journal of Engineering and Applied Sciences. 12: 6895-6903.
- [20] Sendoya-Losada Diego F., Arroyave-Quezada José O. and Velasquez-Pobre Alvaro J. 2019. EPSAC and NEPSAC algorithms applied to a non-linear liquid level system. 2019 IEEE 4th Colombian Conference on Automatic Control (CCAC). IEEE.
- [21] Pulido-Cortes German A., Moreno-Artunduaga Alejandro and Sendoya-Losada Diego F. 2020. Classical and predictive control applied to a non-linear system of coupled tanks. ARPJ Journal of Engineering and Applied Sciences. 15: 1466-1471.